Progress In Electromagnetics Research, Vol. 121, 317–342, 2011

RIGOROUS ANALYSIS OF ELECTROMAGNETIC SCATTERING BY CYLINDRICAL EBG STRUCTURES

V. Jandieri[1, *], K. Yasumoto[2, 3], and Y.-K. Cho[1]

[1]School of Electrical Engineering and Computer Science, Kyungpook National University, Republic of Korea

[2]Computer Science Laboratory, Fukuoka Institute of Technology, 811-0295 Fukuoka, Japan

[3]Kyushu University, Japan

Abstract—Cylindrical EBG structures excited by a Hertzian dipole source and TM polarized plane wave at oblique incidence are analyzed using a rigorous semi-analytical method based on the cylindrical Floquet mode expansion. Concentric and eccentric cylindrical EBG structures are investigated. Resonance and stopband characteristics in the transmission spectra of the cylindrical EBG structures, enhancement and shading effects in the excited fields, radiation patterns of Hertzian dipole located inside the cylindrical EBG structures in both H-plane and E-plane are numerically studied. Co-polarization and cross-polarizations scattering effects between the electric and magnetic fields are investigated at the oblique incidence of plane waves.

1. INTRODUCTION

Periodic dielectric or metallic structures are a subject of continuing interest because of their wide use for practical devices in microwaves and optical waves [1, 2]. Periodic structures are under the growing attention as electromagnetic filters, polarizers, as the components of various devices used in optics and microwave engineering. A periodic array of circular rods is typical of a discrete periodic structure. Various techniques have been developed to formulate the electromagnetic scattering from the planar periodic arrays [3–7]. Recently, we have theoretically investigated radiation of a line source coupled to planar

Received 9 September 2011, Accepted 5 October 2011, Scheduled 31 October 2011

* Corresponding author: Vakhtang Jandieri (jandieri@ee.knu.ac.kr).

EBG structure and explained how the radiation patterns are modified in the presence of EBG structure [8].

An alternative of the planar configuration is a cylindrical array formed by circular rods periodically distributed on a circular ring. Cylindrically periodic structures have received a growing attention because of their potential applications to the designs of photonic crystal fibers [9, 10], directive antennas or beam-switching antennas [11–14]. Recently, we have proposed a semi-analytical approach for two-dimensional electromagnetic scattering, guidance and radiation by the cylindrical arrays. The formulation is rigorous. The method uses three-dimensional T-matrix approach [15], the reflection and transmission matrices of a cylindrical array based on the cylindrical harmonics expansion [16, 17], and the generalized reflection and transmission matrices for a cylindrically layered structure [15, 18]. It should be noted that similar semi-analytical techniques have been reported in [19, 20]. Using the cylindrical harmonic expansion and applying the boundary conditions on each surface of the cylinders, the authors have derived a set of linear equations for unknown scattering coefficients of each individual circular rod. After that, the matrix equation has been directly solved. However, using this technique the number of unknowns increases proportionally to the number of layers and number of circular rods along each layer. In contrast, in our approach, we firstly extract the reflection and transmission matrices of a single cylindrical periodic layer and then obtain the characteristics of the whole layered structure by using a simple recursive formula [15]. Our proposed method could be easily applied to various configurations of the layered cylindrical arrays with different types and locations of the excitation sources. We have applied the method to the modal analysis of guided waves in a specific microstructured optical fiber [21, 22], to the analysis of two-dimensional plane wave scattering by cylindrical structures [17, 23], analysis of line source radiation located inside the cylindrical EBG structures [24] and proofed its accuracy, validity and usefulness. To be best of our knowledge, the rigorous analysis of cylindrical EBG structures has been proposed first time.

In this manuscript, based on the proposed formulation cylindrical EBG structure excited by a Hertzian dipole source and TM polarized plane at oblique incidence is considered. Transmission spectra of *concentric* and *eccentric* configurations of cylindrical EBG structures taking into account all cylindrical Floquet modes and the interaction between the modes are investigated. Resonances and stopband regions of the transmission spectra into several cylindrical modes are numerically studied. It is shown that when the cylindrical EBG of both configurations is obliquely illuminated by plane wave of particular

frequencies related to the resonance frequencies or stopbands, the field patterns are strongly enhanced or shaded inside the cylindrical EBG structure. Discussions about the relation between the resonance and stopband characteristics of the transmission spectra and the excited field patterns inside the cylindrical EBG structure are given. The features may be useful to manipulate the electromagnetic properties of a space by surrounding it with a cylindrical EBG structure. Co-polarization and cross-polarization scattering effects [25] between the electric and magnetic fields at oblique incidence of plane waves on *concentric* and *eccentric* cylindrical EBG structures are also numerically studied. Correctness and accuracy of our solutions has been proved by the test of the optical theorem [26], and comparison with other references for some particular cases.

2. FORMULATION OF THE PROBLEM

Cross sectional view of N-layered cylindrical arrays of circular rods located in a homogeneous background medium with material constants

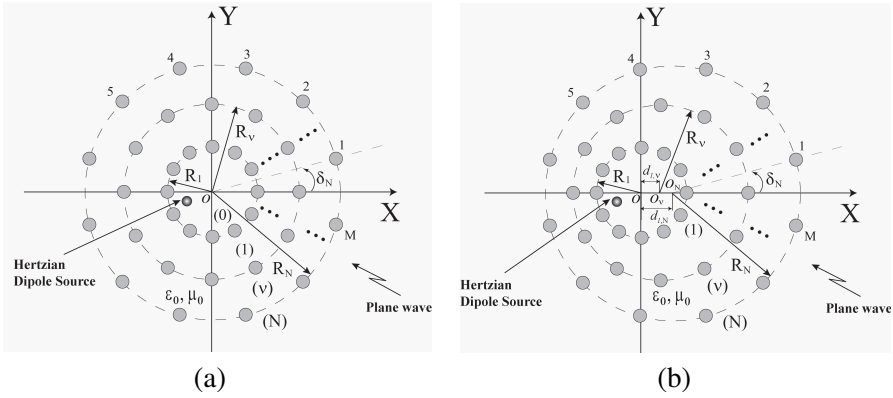

Figure 1. Cross-sectional view of N-layered cylindrical EBG structure formed by M circular rods with radius r_ν periodically distributed on each of N layered: (a) concentric cylindrical arrays, (b) eccentric cylindrical arrays. Radii of the N-layered concentric and eccentric cylindrical surfaces are R_ν ($\nu = 1, 2, 3, \ldots, N$). For eccentric configuration the centre of the 1-st cylindrical layer coincides with the global origin O and a distance between the centers of the 1-st and of the v-th cylindrical layers is $d_{1,\nu}$. Excitation by a Hertzian dipole source placed in the innermost region (0) or a plane wave oblique incidence from the outermost (N) region are considered.

ε_0 and μ_0 is shown in Figure 1. The z dependence of all field components is given as $\exp(i\xi z)$, where ξ is the propagation constant along the z-axis. The rods are infinitely long along the z axis and parallel to each other. The problem is formulated by employing electric E_z and magnetic $\hat{H}_z = (\mu_0/\varepsilon_0)^{1/2} H_z$ fields as the leading fields. Other transversal components of the electric and magnetic fields could be easily defined through E_z and H_z fields.

The M circular rods of radius r_ν and the material constants ε_ν and μ_ν are symmetrically distributed on each of N-layered *concentric* and *eccentric* cylindrical surfaces with radii $R_\nu\,(\nu = 1, 2, 3, \ldots, N)$ as illustrated in Figures 1(a) and 1(b), respectively. The separation angle between nearest two rods along a circular ring is $\theta_M = 2\pi/M$ and δ_ν is an angle of rotation of the cylindrical layers. Region with $R_\nu < \rho < R_{\nu+1}$ is labeled as region (ν) and the innermost region as region (0). For the eccentric configuration (Figure 1(b)) we have assumed that the center of the innermost 1-st cylindrical layer coincides with the global origin O, whereas the centers of other cylindrical layers are displaced along the positive x direction. Distance between the centers of the 1-st and the ν-th layers, 1-st and the N-th layers are $d_{1,\nu}$ and $d_{1,N}$, respectively. Figure 2 shows the detailed configuration of the scattering process through ν-th layer of the cylindrical array. The total field in the (ν)-th region and $(\nu-1)$-th region are expressed

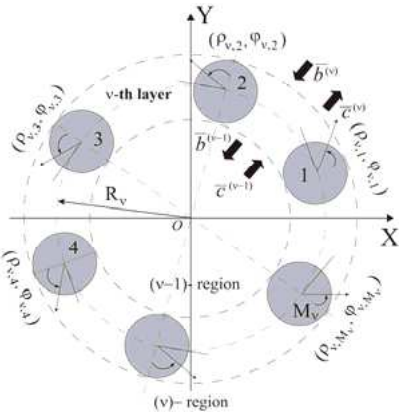

Figure 2. Schematic view of scattering process through the ν-th layer of the cylindrical arrays and local coordinate systems attached to each of M circular rods. $\bar{\mathbf{b}}^{(\nu)}$ and $\bar{\mathbf{c}}^{(\nu)}$ are the amplitude vectors of *incoming* and *outgoing* cylindrical waves, respectively.

in the matrix form as follows:

$$\bar{\psi}^{tot(\nu)} = \bar{\Phi}^T \cdot \bar{\mathbf{b}}^{(\nu)} + \bar{\Psi}^T \cdot \bar{\mathbf{c}}^{(\nu)} \tag{1}$$

$$\bar{\psi}^{tot(\nu-1)} = \bar{\Phi}^T \cdot \bar{\mathbf{b}}^{(\nu-1)} + \bar{\Psi}^T \cdot \bar{\mathbf{c}}^{(\nu-1)} \tag{2}$$

with

$$\bar{\psi}^{tot(\nu)} = \begin{bmatrix} E_z^{(\nu)} \\ \hat{H}_z^{(\nu)} \end{bmatrix}, \quad \bar{\psi}^{tot(\nu-1)} = \begin{bmatrix} E_z^{(\nu-1)} \\ \hat{H}_z^{(\nu-1)} \end{bmatrix} \tag{3}$$

$$\bar{\Phi}^T = \begin{bmatrix} \Phi^T & 0 \\ 0 & \Phi^T \end{bmatrix}, \quad \Phi = [J_m(\kappa\rho)\exp(im\varphi)] \tag{4}$$

$$\bar{\Psi}^T = \begin{bmatrix} \Psi^T & 0 \\ 0 & \Psi^T \end{bmatrix}, \quad \Psi = [H_m^{(1)}(\kappa\rho)\exp(im\varphi)] \tag{5}$$

$$\bar{\mathbf{b}}^{(\nu)} = \begin{bmatrix} \mathbf{b}^{e(\nu)} \\ \mathbf{b}^{h(\nu)} \end{bmatrix}, \quad \bar{\mathbf{c}}^{(\nu)} = \begin{bmatrix} \mathbf{c}^{e(\nu)} \\ \mathbf{c}^{h(\nu)} \end{bmatrix} \tag{6}$$

where $\kappa = \sqrt{k_0^2 - \xi^2}$, J_m and $H_m^{(1)}$ are Bessel and Hankel functions of the m-th order, respectively, $\bar{\mathbf{b}}^{(\nu)}$, $\bar{\mathbf{b}}^{(\nu-1)}$ and $\bar{\mathbf{c}}^{(\nu)}$, $\bar{\mathbf{c}}^{(\nu-1)}$ are the scattering amplitudes of the *incoming* and *outgoing* cylindrical waves on the ν-th layer and $\nu-1$-th layer, respectively and "T" denotes the transpose of the indicated vectors. Using the semi-analytical approach [16, 17, 23], we obtain the following relations between the unknown scattering amplitudes:

$$\begin{aligned} \begin{bmatrix} \mathbf{c}^{e(\nu)} \\ \mathbf{c}^{h(\nu)} \end{bmatrix} &= \bar{\mathbf{R}}_{\nu,\nu-1} \begin{bmatrix} \mathbf{b}^{e(\nu)} \\ \mathbf{b}^{h(\nu)} \end{bmatrix} + \bar{\mathbf{F}}_{\nu,\nu-1} \begin{bmatrix} \mathbf{c}^{e(\nu-1)} \\ \mathbf{c}^{h(\nu-1)} \end{bmatrix} \\ &= \begin{bmatrix} \mathbf{R}_{\nu,\nu-1}^{EE} & \mathbf{R}_{\nu,\nu-1}^{EH} \\ \mathbf{R}_{\nu,\nu-1}^{HE} & \mathbf{R}_{\nu,\nu-1}^{HH} \end{bmatrix} \begin{bmatrix} \mathbf{b}^{e(\nu)} \\ \mathbf{b}^{h(\nu)} \end{bmatrix} \\ &\quad + \begin{bmatrix} \mathbf{F}_{\nu,\nu-1}^{EE} & \mathbf{F}_{\nu,\nu-1}^{EH} \\ \mathbf{F}_{\nu,\nu-1}^{HE} & \mathbf{F}_{\nu,\nu-1}^{HH} \end{bmatrix} \begin{bmatrix} \mathbf{c}^{e(\nu-1)} \\ \mathbf{c}^{h(\nu-1)} \end{bmatrix} \end{aligned} \tag{7}$$

$$\begin{aligned} \begin{bmatrix} \mathbf{b}^{e(\nu-1)} \\ \mathbf{b}^{h(\nu-1)} \end{bmatrix} &= \bar{\mathbf{F}}_{\nu-1,\nu} \begin{bmatrix} \mathbf{b}^{e(\nu)} \\ \mathbf{b}^{h(\nu)} \end{bmatrix} + \bar{\mathbf{R}}_{\nu-1,\nu} \begin{bmatrix} \mathbf{c}^{e(\nu-1)} \\ \mathbf{c}^{h(\nu-1)} \end{bmatrix} \\ &= \begin{bmatrix} \mathbf{F}_{\nu-1,\nu}^{EE} & \mathbf{F}_{\nu-1,\nu}^{EH} \\ \mathbf{F}_{\nu-1,\nu}^{HE} & \mathbf{F}_{\nu-1,\nu}^{HH} \end{bmatrix} \begin{bmatrix} \mathbf{b}^{e(\nu)} \\ \mathbf{b}^{h(\nu)} \end{bmatrix} \\ &\quad + \begin{bmatrix} \mathbf{R}_{\nu-1,\nu}^{EE} & \mathbf{R}_{\nu-1,\nu}^{EH} \\ \mathbf{R}_{\nu-1,\nu}^{HE} & \mathbf{R}_{\nu-1,\nu}^{HH} \end{bmatrix} \begin{bmatrix} \mathbf{c}^{e(\nu-1)} \\ \mathbf{c}^{h(\nu-1)} \end{bmatrix} \end{aligned} \tag{8}$$

where $\bar{\mathbf{R}}_{\nu,\nu-1}$ and $\bar{\mathbf{R}}_{\nu-1,\nu}$ are the reflection matrices of the ν-th layer, which characterize the reflection from the inner region $(\nu-1)$ to the outer region (ν) and from the outer region (ν) to the inner region

$(\nu-1)$, respectively; $\bar{\mathbf{F}}_{\nu-1,\nu}$ and $\bar{\mathbf{F}}_{\nu,\nu-1}$ are the transmission matrices of the ν-th layer that define the transmission from the outer region (ν) to the inner region $(\nu-1)$ and from the inner region $(\nu-1)$ to the outer region (ν), respectively. We have omitted in the paper the detail calculation procedure of the reflection and transmission matrices for the cylindrical layers. The readers can refer to our previously published papers [16, 17, 23, 24]. The closed form of the reflection and transmission matrices are related to the three-dimensional T-matrix of a single circular rod in isolation located on the ν-th circular ring [15], and the geometrical parameters characterizing the periodic distribution of the circular rods along the cylindrical layers. The reflection $\bar{\mathbf{R}}_{\nu,\nu-1}$, $\bar{\mathbf{R}}_{\nu-1,\nu}$ and transmission $\bar{\mathbf{F}}_{\nu-1,\nu}$, $\bar{\mathbf{F}}_{\nu,\nu-1}$ matrices consist of four block matrices. The diagonal block matrices $\{\mathbf{R}^{EE}_{\nu,\nu-1}, \mathbf{R}^{HH}_{\nu,\nu-1}\}$, $\{\mathbf{R}^{EE}_{\nu-1,\nu}, \mathbf{R}^{HH}_{\nu-1,\nu}\}$ and $\{\mathbf{F}^{EE}_{\nu,\nu-1}, \mathbf{F}^{HH}_{\nu,\nu-1}\}$, $\{\mathbf{F}^{EE}_{\nu-1,\nu}, \mathbf{F}^{HH}_{\nu-1,\nu}\}$ represent the reflection and transmission into the co-polarized electric and magnetic fields, while the non-diagonal block matrices $\{\mathbf{R}^{EH}_{\nu,\nu-1}, \mathbf{R}^{HE}_{\nu,\nu-1}\}$, $\{\mathbf{R}^{EH}_{\nu-1,\nu}, \mathbf{R}^{HE}_{\nu-1,\nu}\}$ and $\{\mathbf{F}^{EH}_{\nu,\nu-1}, \mathbf{F}^{HE}_{\nu,\nu-1}\}$, $\{\mathbf{F}^{EH}_{\nu-1,\nu}, \mathbf{F}^{HE}_{\nu-1,\nu}\}$ describe the reflection and transmission into the cross-polarization space-harmonic components. In case of dielectric scatterers both co-polarized and cross-polarized fields give the contribution in the formation of the scattered field, however in case of perfect conductor scatterers, the cross-polarization scattering effect disappears and the problem is reduced to the consideration of TM and TE waves, separately.

3. EXCITATION BY HERTZIAN DIPOLE SOURCE

Let us consider that Hertzian dipole source located in the innermost (0) region at $(d_s,\ \phi_s,\ 0)$ is directed in z direction. Using the Fourier integral representation, the source field in the local coordinate $(\rho_s,\ \varphi_s,\ z)$ is given as:

$$E^i_z = \frac{1}{2\pi}\int\limits_{-\infty}^{\infty} \tilde{E}^i_z(\rho_s,\xi)\exp(i\xi z)d\xi, \quad H^i_z = 0 \tag{9}$$

with

$$\tilde{E}^i_z(\rho_s,\xi) = -\frac{\omega\mu_0 I\ell}{4}\frac{\kappa^2}{k^2}H^{(1)}_0(\kappa\rho_s) \tag{10}$$

where $\kappa = \sqrt{k_0^2-\xi^2}$, ξ is the propagation constant along the z-axis, and $I\ell$ is the current moment of the electric dipole. Using the Graf's addition theorem [27], the source field in the spectral domain (9) is

expressed in the global coordinate system (ρ, φ) as follows:

$$\tilde{E}_z^i(\rho,\varphi,\xi) = -\frac{\omega\mu_0 I\ell}{4}\frac{\kappa^2}{k^2}\Psi^T \cdot \mathbf{s}^e \tag{11}$$

with

$$\mathbf{s}^e = \left[J_m(\kappa d_s)\exp(-im\phi_s)\right]. \tag{12}$$

where $\mathbf{s}^e$ is the spectral amplitude of the source field. Following the same calculation procedure as presented in [16], the transmitted fields $E_z^{t(N)}$ and $\hat{H}_z^{t(N)}$ in the far-zone are obtained as:

$$\begin{aligned}\begin{bmatrix} E_z^{t(N)} \\ \hat{H}_z^{t(N)} \end{bmatrix} &= -\frac{\omega\mu_0 I\ell}{4}\frac{\exp(ikr)}{\pi r}\sin^2\theta \sum_{m=-\infty}^{\infty}\exp(im\varphi) \\ &\quad \exp\left[-i(2m+1)\frac{\pi}{4}\right]\begin{bmatrix} \mathbf{c}_m(\xi)^{e(N)} \\ \mathbf{c}_m(\xi)^{h(N)} \end{bmatrix}_{\xi=k_0\cos\theta}\end{aligned} \tag{13}$$

where $\{\mathbf{c}_m(\xi)^{e(N)}\}$ and $\{\mathbf{c}_m(\xi)^{h(N)}\}$ are the spectral scattering amplitudes in the outermost (N) region of $E_z^{(N)}$ and $\hat{H}_z^{(N)}$ fields, respectively and (r,φ,θ) denote the location of an observation point with respect to the global origin O. The scattering amplitudes $\{\mathbf{c}_m(\xi)^{e(N)}\}$ and $\{\mathbf{c}_m(\xi)^{h(N)}\}$ are related to the amplitude of the source field $\{\mathbf{s}_m^e(\xi)\}$ in the (0) region through the generalized transmission matrix $\tilde{\bar{\mathbf{F}}}_{N,0}$:

$$\begin{bmatrix} \mathbf{c}_m(\xi)^{e(N)} \\ \mathbf{c}_m(\xi)^{h(N)} \end{bmatrix} = \tilde{\bar{\mathbf{F}}}_{N,0}\begin{bmatrix} s_m^e(\xi) \\ 0 \end{bmatrix} \tag{14}$$

where

$$\tilde{\bar{\mathbf{F}}}_{N,0} = \bar{\mathbf{F}}_{N,N-1}\cdot\bar{\Gamma}_{N-1,N-2}\ldots\bar{\Gamma}_{\nu,\nu-1}\ldots\bar{\Gamma}_{1,0} \tag{15}$$

$$\begin{aligned}\bar{\Gamma}_{\nu,\nu-1} &= \left(\mathbf{I} - \bar{\mathbf{U}}_{\nu-1,\nu}^{-1}\cdot\bar{\mathbf{R}}_{\nu,\nu-1}\cdot\bar{\mathbf{U}}_{\nu-1,\nu}\cdot\tilde{\bar{\mathbf{R}}}_{\nu,\nu+1}\right)^{-1} \\ &\quad \cdot\bar{\mathbf{U}}_{\nu-1,\nu}^{-1}\cdot\bar{\mathbf{F}}_{\nu,\nu-1}\end{aligned} \tag{16}$$

$$\begin{aligned}\tilde{\bar{\mathbf{R}}}_{v,v+1} &= \bar{\mathbf{R}}_{v,v+1} + \bar{\mathbf{F}}_{v,v+1}\cdot\bar{\mathbf{U}}_{\nu-1,\nu}\cdot\tilde{\bar{\mathbf{R}}}_{\nu+1,\nu+2} \\ &\quad \cdot\left(\bar{\mathbf{I}} - \bar{\mathbf{U}}_{\nu-1,\nu}^{-1}\cdot\bar{\mathbf{R}}_{\nu+1,\nu}\cdot\bar{\mathbf{U}}_{\nu-1,\nu}\cdot\tilde{\bar{\mathbf{R}}}_{\nu+1,\nu+2}\right)^{-1} \\ &\quad \cdot\bar{\mathbf{U}}_{\nu-1,\nu}^{-1}\cdot\bar{\mathbf{F}}_{v+1,\nu}\end{aligned} \tag{17}$$

$$\bar{\mathbf{U}}_{\nu-1,\nu} = \begin{bmatrix} \mathbf{U}_{\nu-1,\nu} & 0 \\ 0 & \mathbf{U}_{\nu-1,\nu} \end{bmatrix}, \quad \mathbf{U}_{\nu-1,\nu} = \{J_{m-n}(\kappa d_{\nu-1,\nu})\} \tag{18}$$

$$\bar{\mathbf{I}} = \begin{bmatrix} \mathbf{I} & 0 \\ 0 & \mathbf{I} \end{bmatrix}, \quad \mathbf{I} = [\delta_{mm'}] \tag{19}$$

Here $\tilde{\tilde{\mathbf{R}}}_{v,v+1}$ denotes the generalized reflection matrix viewed from the (ν)-th region to the whole outer region and it is calculated through the N times recursion process starting with $\tilde{\tilde{\mathbf{R}}}_{N,N+1} = 0$. $\mathbf{I}$ is the unit matrix. In (18) $d_{\nu-1,\nu}$ denotes a distance between the centers $O_{\nu-1}$, O_ν of $\nu-1$-th and ν-th cylindrical layers for the *eccentric* configuration shown in Figure 1(b). If $d_{\nu-1,\nu} = 0$, we have $\bar{\mathbf{U}}_{\nu-1,\nu} = \bar{\mathbf{I}}$ and (14)–(17) reduce to the expressions for the *concentric* configuration of cylindrical EBG structure (Figure 1(a)).

4. EXCITATION BY PLANE WAVE AT OBLIQUE INCIDENCE

Let us consider a plane wave of unit amplitude with a wavevector $\mathbf{k}_0$ is obliquely incident from the outermost region (N) on the cylindrical structure, where $\mathbf{k}_0 = (k_0, \theta^i, \varphi^i)$ is the spherical coordinate system with the origin O, $k_0 = 2\pi/\lambda$ and λ is the wavelength in the free space. The z components of the incident field are expressed in the cylindrical coordinate system (ρ, φ) as follows:

$$\bar{\psi}^{i(N)} = \bar{\Phi}^T \cdot \bar{\mathbf{b}}^{(N)} \tag{20}$$

with

$$\bar{\psi}^{i(N)} = \begin{bmatrix} E_z^{i(N)} \\ \hat{H}_z^{i(N)} \end{bmatrix} \tag{21}$$

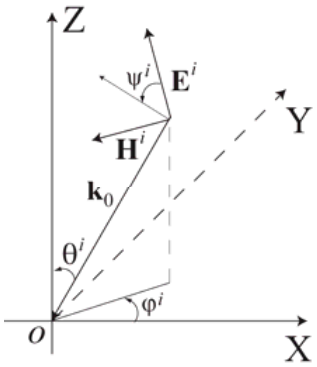

Figure 3. Oblique incidence of plane waves, where (θ^i, φ^i) denotes the angle of incidence in spherical coordinate system and ψ^i is polarization angle of the incident electric field.

$$\bar{\mathbf{b}}^{(N)} = \begin{bmatrix} \mathbf{b}^{e(N)} \\ \mathbf{b}^{h(N)} \end{bmatrix} \tag{22}$$

$$\mathbf{b}^{e(N)} = \exp(i\xi z)\sin\theta^i \cos\psi^i \mathbf{s} \tag{23}$$

$$\mathbf{b}^{h(N)} = \exp(i\xi z)\sin\theta^i \sin\psi^i \mathbf{s} \tag{24}$$

$$\mathbf{s} = \left[i^m \exp(-im\varphi^i)\right] \tag{25}$$

where $\kappa = \sqrt{k_0^2 - \xi^2}$, $\xi = k_0 \cos\theta^i$ and ψ^i is the polarization angle of the incident electric field as depicted in Figure 3. By tracing the scattering process (Figure 2) over the layered cylindrical arrays, the generalized reflection matrices $\bar{\bar{\mathbf{R}}}_{\nu,\nu-1}$ viewed from region (ν) to all of the inner regions could be obtained as follows:

$$\begin{aligned} \bar{\bar{\mathbf{R}}}_{\nu,\nu-1} \;=\; & \bar{\mathbf{U}}^{-1}_{\nu-1,\nu}\bar{\mathbf{R}}_{\nu,\nu-1}\bar{\mathbf{U}}_{\nu-1,\nu} + \bar{\mathbf{U}}^{-1}_{\nu-1,\nu}\bar{\mathbf{F}}_{\nu,\nu-1} \\ & \left(\bar{\mathbf{I}} - \bar{\bar{\mathbf{R}}}_{\nu-1,\nu-2}\bar{\mathbf{R}}_{\nu-1,\nu}\right)^{-1} \bar{\bar{\mathbf{R}}}_{\nu-1,\nu-2}\bar{\mathbf{F}}_{\nu-1,\nu}\bar{\mathbf{U}}_{\nu-1,\nu} \end{aligned} \tag{26}$$

The generalized reflection matrix $\bar{\bar{\mathbf{R}}}_{\nu,\nu-1}$ could be calculated through the N times recursion process starting with $\bar{\bar{\mathbf{R}}}_{2,1} = \bar{\mathbf{R}}_{2,1}$. Since the reflection $\bar{\mathbf{R}}_{\nu,\nu-1}$, $\bar{\mathbf{R}}_{\nu-1,\nu}$ and transmission $\bar{\mathbf{F}}_{\nu-1,\nu}$, $\bar{\mathbf{F}}_{\nu,\nu-1}$ matrices for each cylindrical array and the generalized reflection matrix $\bar{\bar{\mathbf{R}}}_{\nu,\nu-1}$ for the N-layered cylindrical structure are derived, the total field in each region of the cylindrical structure could be defined. The total field in the outermost (N)-th region is expressed as:

$$\bar{\psi}^{tot(N)} = \left(\bar{\Phi}^T \cdot \bar{\mathbf{U}}_{1,N} + \bar{\Psi}^T \cdot \bar{\mathbf{U}}_{1,N} \cdot \bar{\bar{\mathbf{R}}}_{N,N-1}\right) \cdot \bar{\mathbf{b}}^{(N)} \tag{27}$$

In the (ν)-th region inside the cylindrical structure, the total field is given by the following expression:

$$\bar{\psi}^{tot(\nu)} = (\bar{\Phi}^T \cdot \bar{\mathbf{U}}_{1,\nu} + \bar{\Psi}^T \cdot \bar{\mathbf{U}}_{1,\nu} \cdot \bar{\bar{\mathbf{R}}}_{\nu,\nu-1}) \cdot \bar{\bar{\mathbf{F}}}_{\nu,N} \cdot \bar{\mathbf{b}}^{(N)} \tag{28}$$

where

$$\bar{\bar{\mathbf{F}}}_{\nu,N} = \bar{\Lambda}_{\nu,\nu+1} \cdot \bar{\Lambda}_{\nu+1,\nu+2} \ldots \bar{\Lambda}_{N-1,N} \tag{29}$$

$$\bar{\Lambda}_{\nu,\nu+1} = (\bar{\mathbf{I}} - \bar{\mathbf{R}}_{\nu,\nu+1} \cdot \bar{\bar{\mathbf{R}}}_{\nu,\nu-1})^{-1} \cdot \bar{\mathbf{F}}_{\nu,\nu+1} \cdot \bar{\mathbf{U}}_{\nu,\nu+1} \tag{30}$$

Transmitted field in the innermost (0)-th region is given as:

$$\bar{\psi}^{tot(0)} = \bar{\Phi}^T \cdot \bar{\bar{\mathbf{F}}}_{0,N} \cdot \bar{\mathbf{b}}^{(N)} \tag{31}$$

Here $\bar{\bar{\mathbf{F}}}_{0,N}$ is the generalized transmission matrix in the innermost (0) region from the outermost (N) region. If $d_{\nu-1,\nu} = 0$, we have $\bar{\mathbf{U}}_{\nu-1,\nu} = \bar{\mathbf{I}}$ and (26)–(31) reduce to the expressions for *concentric* configuration of cylindrical EBG structure (Figure 1(a)).

5. NUMERICAL RESULTS AND DISCUSSIONS

Although a substantial number of numerical results could be generated for different configurations of cylindrical EBG structures, for the numerical analysis we consider two different *concentric* and *eccentric* configurations of three-layered ($N = 3$) cylindrical EBG structures composed of $M_1 = M_2 = M_3 = 8$ identical circular rods $r_1 = r_2 = r_3 = 0.15R_1$ periodically distributed along each cylindrical layer having radii R_1, $R_2 = 2R_1$, $R_3 = 3R_1$ and $\delta_1 = \delta_2 = \delta_3 = 0°$. In case of *eccentric* cylindrical configuration, we assume that $O_1O_2 = O_2O_3 = 0.4R_1$. Firstly, we numerically investigate the spectral responses of both *concentric* and *eccentric* cylindrical structures in terms of the generalized transmission matrix $\tilde{\tilde{\mathbf{F}}}_{N,0}(\omega, \theta)$ given in (14)–(19). The circular rods are assumed to be perfect conductors.

When the Hertzian dipole source is located at the global origin O of *concentric* cylindrical EBG structure, the structure is symmetric viewed from the origin O and only (0, 0), (±8, 0), (±16, 0) elements contribute in the excitation of the lowest principle cylindrical Floquet modes [29]. Figure 4 shows the dependence of the generalized

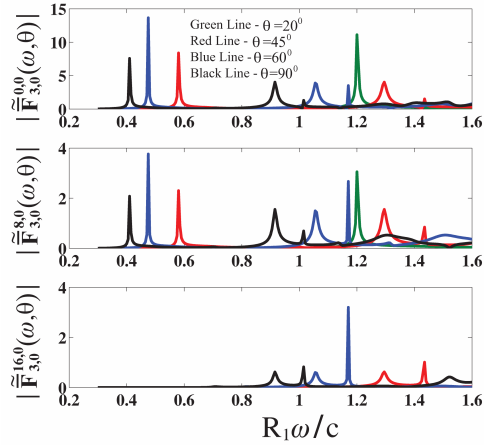

Figure 4. Frequency response of the generalized transmission matrix $|\tilde{\tilde{\mathbf{F}}}^{m,0}_{3,0}(\omega, \theta)|$ for three layered *concentric* cylindrical EBG structure composed of eight perfect conductor circular rods ($r_1 = r_2 = r_3 = 0.15R_1$) periodically distributed along each cylindrical layer having radii R_1, $R_2 = 2R_1$, $R_3 = 3R_1$. Note that $|\tilde{\tilde{\mathbf{F}}}^{m,0}_{3,0}(\omega, \theta)| = |\tilde{\tilde{\mathbf{F}}}^{-m,0}_{3,0}(\omega, \theta)|$. Green line — $\theta = 20°$; red line — $\theta = 45°$; blue line — $\theta = 60°$; black line — $\theta = 90°$.

transmission matrix $|\tilde{\tilde{\mathbf{F}}}_{3,0}^{m,0}(\omega,\theta)|$ as a function of $R_1\omega/c$, where $\tilde{\tilde{F}}_{3,0}^{m,0}(\omega,\theta)$ represents $(m,\ 0)$ elements of matrix $\tilde{\tilde{\mathbf{F}}}_{3,0}(\omega,\theta)$. From Figure 4 we can see that there exist a series of stopband and passband for each of the excited cylindrical mode. The transmission is very small in the stopband regions, whereas sharp resonance peaks appear in the passband regions. The main resonances occur at $R_1\omega/c = 0.41$ and $R_1\omega/c = 0.915$ for $\theta = 90^\circ$ (black line), at $R_1\omega/c = 0.475$, $R_1\omega/c = 1.055$ and $R_1\omega/c = 1.17$ for $\theta = 60^\circ$ (blue line), at $R_1\omega/c = 0.58$ and $R_1\omega/c = 1.295$ for $\theta = 45^\circ$ (red line) and at $R_1\omega/c = 1.2$ for $\theta = 20^\circ$ (green line).

Firstly, we study the total field distributions inside the *concentric* cylindrical EBG structure illuminated by obliquely incident TM

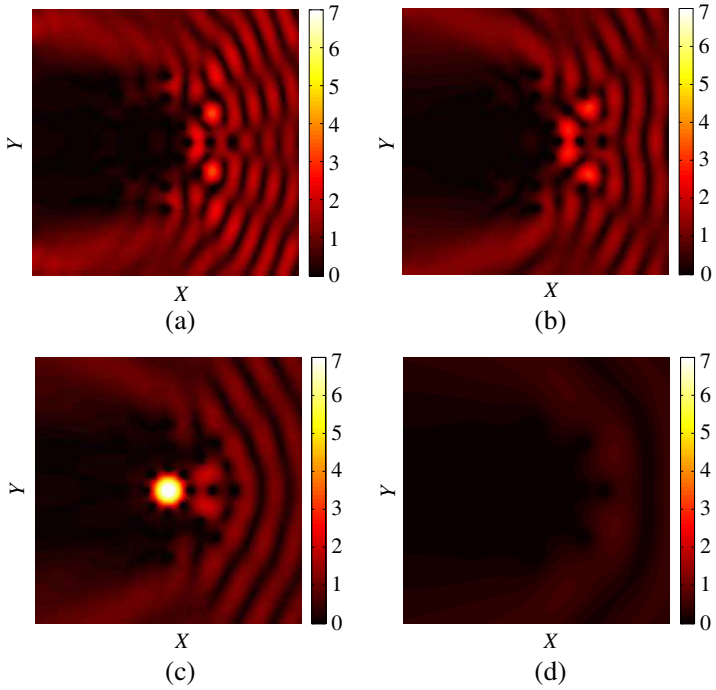

Figure 5. Total field distribution of the three layered $(N = 3)$ *concentric* cylindrical EBG structure composed of eight $(M = 8)$ perfect conductor circular rods $(r_1 = r_2 = r_3 = 0.15R_1)$ periodically distributed along each layer having radii R_1, $R_2 = 2R_1$, $R_3 = 3R_1$ for the excitation of oblique incidence TM plane wave at $R_1\omega/c = 0.58$: (a) $\theta^i = 90^\circ$, (b) $\theta^i = 60^\circ$, (c) $\theta^i = 45^\circ$ and (d) $\theta^i = 20^\circ$; $\varphi^i = 180^\circ$.

polarized plane wave $\psi^i = 0°$ when $\varphi^i = 180°$. Figure 5 shows the total field distribution at the normalized excitation frequency $R_1\omega/c = 0.58$, which corresponds to the resonance frequency for $|\tilde{\tilde{\mathbf{F}}}^{0,0}_{3,0}(\omega, \theta = 45°)|$ and $|\tilde{\tilde{\mathbf{F}}}^{8,0}_{3,0}(\omega, \theta = 45°)|$ as presented in Figure 4 (red line). On the other hand, $R_1\omega/c = 0.58$ lies in a stopband region for other cylindrical Floquet modes. Since $|\tilde{\tilde{\mathbf{F}}}^{0,0}_{3,0}(\omega, \theta = 45°)| \gg |\tilde{\tilde{\mathbf{F}}}^{8,0}_{3,0}(\omega, \theta = 45°)|$ we can see that a strong enhancement of the field intensity is observed at the oblique incidence of TM plane wave for $\theta^i = 45°$ and a focused field pattern is formed in the innermost region of the *concentric* cylindrical EBG structure (Figure 5(c)). Note that at the other angles of θ^i the innermost region of the cylindrical EBG structure is shaded because of the stopband nature of the structure.

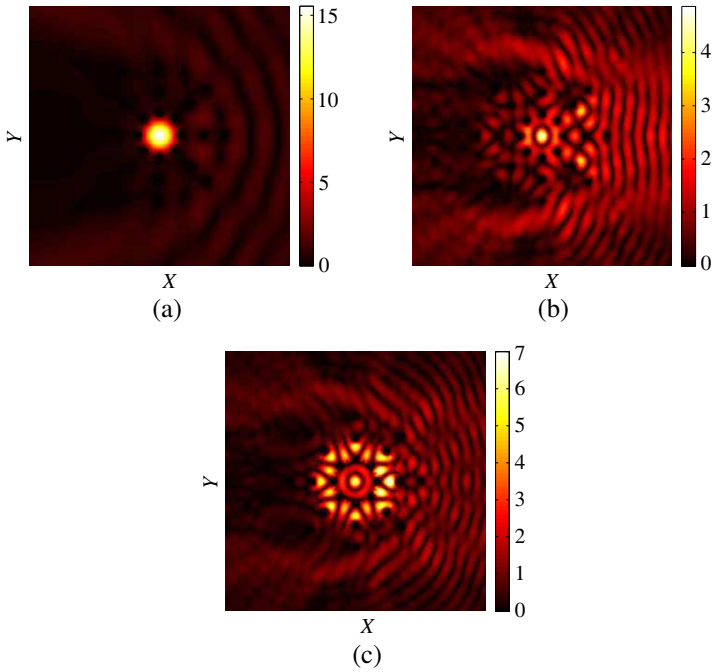

Figure 6. Total field distribution of the three layered ($N = 3$) *concentric* cylindrical EBG structure composed of eight ($M = 8$) perfect conductor circular rods ($r_1 = r_2 = r_3 = 0.15R_1$) periodically distributed along each layer having radii R_1, $R_2 = 2R_1$, $R_3 = 3R_1$ for the excitation of oblique incidence TM plane wave $\theta^i = 60°$ at: (a) $R_1\omega/c = 0.475$, (b) $R_1\omega/c = 1.055$, (c) $R_1\omega/c = 1.17$.

In Figure 6 we present the total field distributions of the *concentric* cylindrical EBG structure obliquely illuminated by the TM polarized plane wave $\theta^i = 60°$ at the normalized excitation frequencies $R_1\omega/c = 0.475$, $R_1\omega/c = 1.055$ and $R_1\omega/c = 1.17$, which correspond to the resonance frequencies for $|\tilde{\tilde{\mathbf{F}}}^{0,0}_{3,0}(\omega, \theta = 60°)|$, $|\tilde{\tilde{\mathbf{F}}}^{8,0}_{3,0}(\omega, \theta = 60°)|$ and $|\tilde{\tilde{\mathbf{F}}}^{16,0}_{3,0}(\omega, \theta = 60°)|$ (blue line in Figure 4). It could be seen that the interference between the resonated cylindrical modes produces a strong focused field pattern in the innermost region (Figures 6(a), 6(b)) and a unique field pattern with 16 maxima between the first and second layers of the *concentric* cylindrical EBG structure (Figure 6(c)). The appearance of field pattern with 16 maxima at $R_1\omega/c = 1.17$ could be explained by the strong contribution of (16, 0) cylindrical mode in the formation of the field (Figure 4).

Next, we numerically investigate the resonance and stopband characteristics of *eccentric* cylindrical EBG structures in terms of the frequency responses of the generalized transmission matrix $\tilde{\tilde{\mathbf{F}}}_{N,0}(\omega, \theta)$ given in (14)–(19). Hertzian dipole source is located at the global origin O of *eccentric* cylindrical EBG structure, which coincides with the centre of the 1-st cylindrical layer. It should be mentioned that comparison to the *concentric* configuration, the *eccentric* cylindrical EBG structure is not symmetric viewed from the origin O and all cylindrical Floquet modes $m = 0, \pm1, \pm2, \pm3, \ldots$; $n = 0$ are excited.

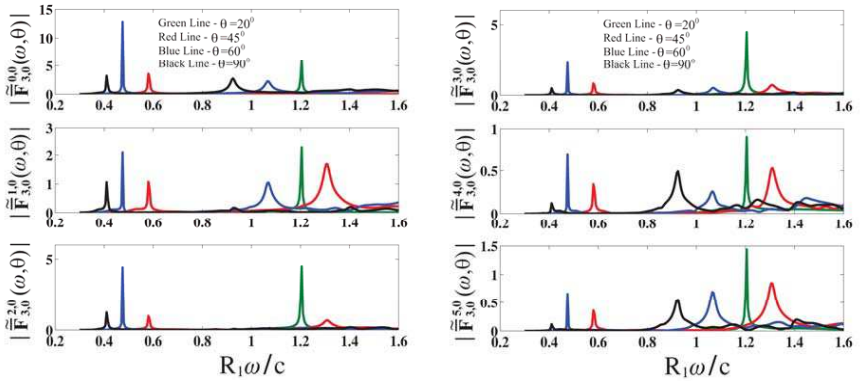

Figure 7. Frequency response of the generalized transmission matrix $|\tilde{\tilde{\mathbf{F}}}^{m,0}_{3,0}(\omega, \theta)|$ of the lowest six cylindrical modes for *eccentric* cylindrical EBG structure $O_1O_2 = O_2O_3 = 0.4R_1$. Other parameters are the same as those in Figure 4.

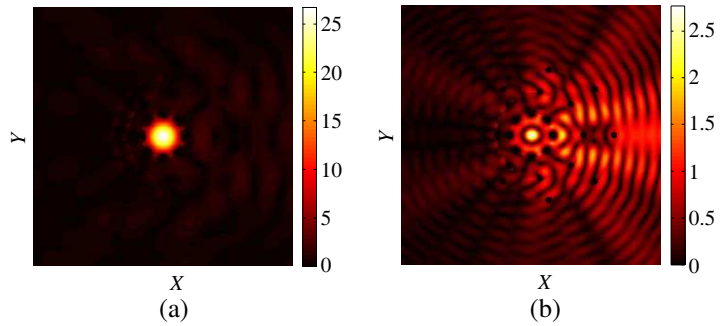

Figure 8. Total field distribution of the three layered ($N = 3$) *eccentric* cylindrical EBG structure $O_1O_2 = O_2O_3 = 0.4R_1$ for the excitation of oblique incidence TM plane wave $\theta^i = 60^0$ at: (a) $R_1\omega/c = 0.475$, (b) $R_1\omega/c = 1.055$. Other parameters are the same as those in Figure 6.

Figure 7 shows the dependence of the generalized transmission matrix $|\tilde{\tilde{\mathbf{F}}}^{m,0}_{3,0}(\omega,\theta)|$ as a function of $R_1\omega/c$ for the lowest six cylindrical Floquet modes. From Figure 7 we could see that the most of the resonance peaks are at the same frequencies as those for *concentric* configuration, however the peaks' maxima are different. Note that the resonance peak at $R_1\omega/c = 1.17$ for the *concentric* configuration (Figure 4), which contributed in the formation of a unique field pattern in Figure 6(c), is not observed in case of *eccentric* configuration. In Figure 8 the total field distributions of the *eccentric* cylindrical EBG structure illuminated by the TM polarized plane wave $\theta^i = 60^\circ$ at the normalized excitation frequencies $R_1\omega/c = 0.475$ and $R_1\omega/c = 1.055$ are presented and compared to those in Figure 6 for *concentric* configuration. From Figure 8 it could be seen that the total field intensity is greatly enhanced in the innermost region at $R_1\omega/c = 0.475$, whereas it slightly decreases at $R_1\omega/c = 1.055$. It could be explained by the interference of the cylindrical Floquet modes at particular resonance frequencies (Figure 7).

Next, we investigate the radiation pattern of a Hertzian dipole source located inside the *concentric* cylindrical EBG structure in both principle H-plane and E-plane. The geometry of the problem is the same as for Figures 4–6. The radiation patterns in both H-plane and E-plane are presented in Figures 9 and 10 for two resonance frequencies $R_1\omega/c = 0.41, 0.915$ at $\theta = 90^\circ$ (principle H-plane), when the Hertzian dipole is located at the origin of the cylindrical EBG structure $d_s = 0$. At $R_1\omega/c = 0.41$ (dashed line) the radiation pattern in H-plane is almost omnidirectional. It could be explained by the fact that the absolute value of the (0, 0) component of the generalized transmission

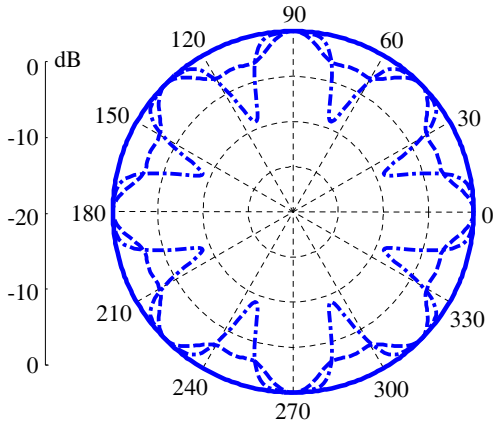

Figure 9. Radiation patterns of hertzian dipole in H-plane at two resonance frequencies for $\theta = 90°$ (Figure 4) of *concentric* cylindrical EBG structure: $R_1\omega/c = 0.41$ (dashed line) and $R_1\omega/c = 0.915$ (dashed-dotted line). Radiation pattern of hertzian dipole without cylindrical EBG (solid line).

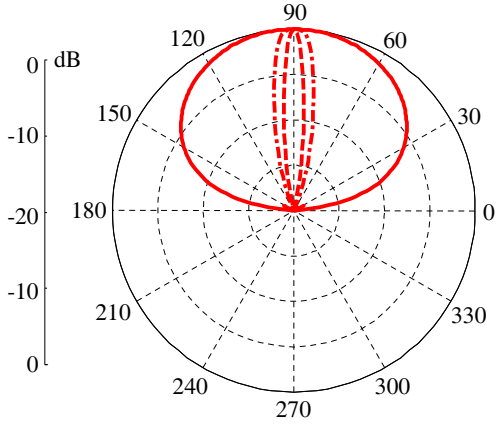

Figure 10. The same as in Figure 9 in E-plane.

matrix is much greater than that for the excited higher order cylindrical Floquet modes $|\tilde{\tilde{\mathbf{F}}}^{0,0}_{3,0}(\omega, \theta = 90°)| \gg |\tilde{\tilde{\mathbf{F}}}^{8,0}_{3,0}(\omega, \theta = 90°)|$. Note that if $(\pm 8,\ 0)$ mode of the generalized transmission matrix were almost zero $|\tilde{\tilde{\mathbf{F}}}^{8,0}_{3,0}(\omega, \theta = 90°)| \approx 0$, completely omnidirectional radiation pattern would be formed [29], since radiated field would not contain any term with φ dependence. At $R_1\omega/c = 0.915$ (dashed-dotted line)

the radiation pattern with 8 beams is formed, since the higher order modes $(\pm 8, 0)$, $(\pm 16, 0)$ also give the contribution in the formation of the radiated field. However, the multibeam effect is not substantial. This is because $|\tilde{\tilde{\mathbf{F}}}^{0,0}_{3,0}(\omega, \theta = 90^\circ)|$ is a big value at $R_1\omega/c = 0.915$ and it compensates the effect of interaction of the higher order modes to form the strongly directive multibeam radiation pattern. Despite the fact that the proposed cylindrical EBG structure could not be considered as an appropriate structure from the viewpoint of design the multibeam antenna, our analysis have demonstrated the principles of the formation of multibeam radiation pattern of Hertzian dipole source and shown that the directivity of radiation of a Hertzian dipole is closely related to the resonance characteristics in the transmission spectra of the cylindrical EBG structure. The results are not presented here, however, it should be mentioned that for realization of the multibeam radiation pattern with 8 narrow beams in H-plane in the presence of cylindrical EBG structure, it would be better to increase the number of circular rods along the second and third cylindrical layers such as $M_2 = 2M_1 = 16$, $M_3 = 3M_1 = 24$ [29]. Interestingly, narrow beam radiation patterns in the vertical direction are formed at both resonance frequencies in E-plane ($\varphi = \varphi_{\max}$) as presented in Figure 10. For comparison the radiation patterns of Hertzian dipole source without the cylindrical EBG structures are also plotted by a solid line in both principle planes.

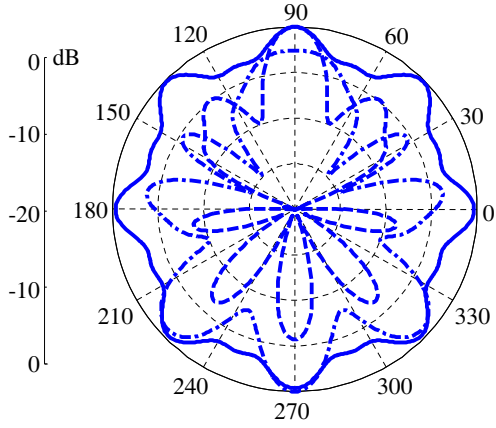

Figure 11. Radiation patterns of Hertzian dipole in H-plane at two resonance frequencies (Figure 4) of *concentric* cylindrical EBG structure: $R_1\omega/c = 0.41$ (solid line), $R_1\omega/c = 0.475$ (dashed-dotted line) and $R_1\omega/c = 0.58$ (dashed line).

Figures 11 and 12 illustrate the radiation pattern of Hertzian dipole located at a distance $d_s/R_1 = 0.8$ from the origin in the innermost region of *concentric* cylindrical EBG structure. We should mention that when the excitation source is not located at the origin, all the components of the generalized transmission matrix give contribution in the formation of the radiated field. Note that in the previous case, when the source was located at the origin $d_s = 0$, only $|\tilde{\tilde{\mathbf{F}}}^{m,0}_{3,0}(\omega,\theta)|$, $m = \pm 8, \pm 16, \pm 24, \ldots$ components have been taken into account. We consider three normalized frequencies $R_1\omega/c = 0.41$, 0.475, 0.58, which correspond to three lowest resonance frequencies for $\theta = 90°$, $\theta = 60°$ and $\theta = 45°$, respectively (Figure 4). As it could be expected, very narrow directive patterns are observed in E-plane along $\theta = 90°$, $\theta = 60°$ and $\theta = 45°$ at these particular frequencies plotted by solid, dashed-dotted and dashed lines, respectively. However, no directive radiation patterns are formed in principle H-plane (Figure 11). In order to improve the radiation pattern in H-plane we placed one additional circular rod of perfect conductor having radius $r_{orig}/R_1 = 0.2$ at the origin of the cylindrical EBG structure. This circular rod could serve as a ground plane for cylindrical EBG structure. Please note that reflection matrix of this circular rod is just a diagonal T-matrix of a circular rod in isolation. From Figure 13 it follows that the radiation pattern in H-plane is substantially improved and very fine radiation patterns are formed in vertical direction. As for E-plane shown in Figure 14, the radiation patterns are changed comparison to Figure 12 by the interaction with the circular rod placed at the origin. Three directive radiation pattern

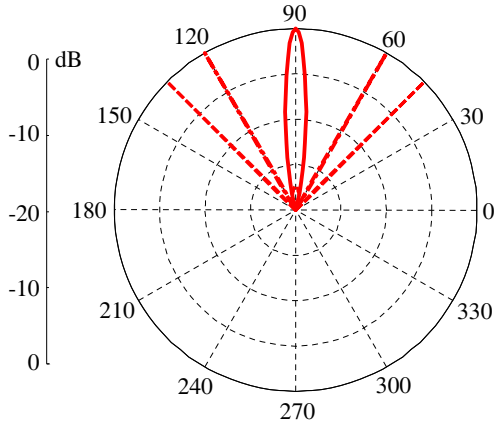

Figure 12. The same as in Figure 11 in E-plane.

are formed in the vertical direction, whose Full Width at Half Maxima (FWHM) are approximately 60 degree.

Finally, we study in some detail the co-polarization and cross-polarization scattering characteristics between the electric and magnetic fields at the oblique incidence of plane waves on the cylindrical EBG structures. Geometry of the problem is the same as for Figures 4–8. Using the asymptotic behavior of cylindrical Hankel function in (27), the scattered fields in the far-zone $\kappa\rho \gg 1$ is expressed

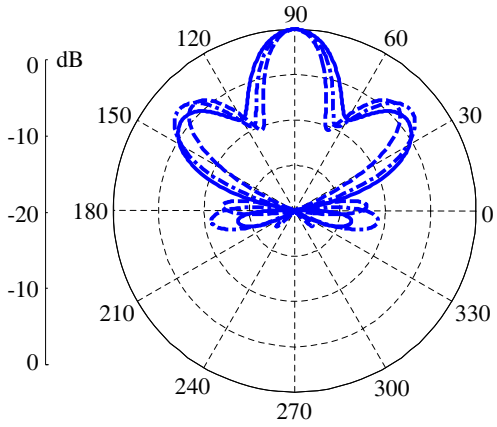

Figure 13. The same as in Figure 11, but one additional perfect conductor circular rod having radius $r_{orig}/R_1 = 0.2$ is placed at the origin of concentric cylindrical EBG structure.

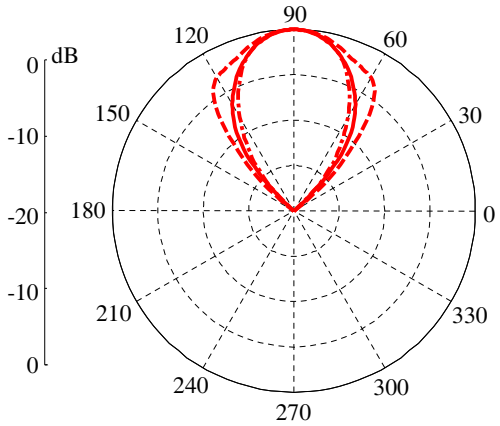

Figure 14. The same as in Figure 13 in E-plane.

as follows:

$$\begin{bmatrix} E_z^s \\ \hat{H}_z^s \end{bmatrix} \simeq \begin{bmatrix} f^e(\varphi,\, \theta^i,\, \varphi^i) \\ f^h(\varphi,\, \theta^i,\, \varphi^i) \end{bmatrix} \frac{\exp(\kappa\rho)}{\sqrt{\rho}} \tag{32}$$

where

$$f^e(\varphi,\theta^i,\varphi^i) = \frac{1-i}{\sqrt{\pi k_0 \sin\theta^i}} \left(\sum_{m,n} (-i)^m \exp(im\varphi) R^{EE}_{N,N-1;mn} b_n^{e(N)} + \sum_{m,n} (-i)^m \exp(im\varphi) R^{EH}_{N,N-1;mn} b_n^{h(N)} \right) \tag{33}$$

$$f^h(\varphi,\theta^i,\varphi^i) = \frac{1-i}{\sqrt{\pi k_0 \sin\theta^i}} \left(\sum_{m,n} (-i)^m \exp(im\varphi) R^{HE}_{N,N-1;mn} b_n^{e(N)} + \sum_{m,n} (-i)^m \exp(im\varphi) R^{HH}_{N,N-1;mn} b_n^{h(N)} \right) \tag{34}$$

Here $b_n^{e(N)}$ and $b_n^{h(N)}$ are the amplitudes of the incident fields given by (20)–(25). Note that the scattering amplitudes in (33), (34) are expressed through the generalized reflection matrices of both co-polarized and cross-polarized space harmonics. In the numerical results the normalized frequency parameter is $R_1/\lambda = 0.7$ and $\varphi^i = 180^\circ$. In Figures 15–18 we plot the normalized differential scattering cross-section:

$$\begin{aligned} k_0\sigma &= 2\pi \frac{1}{\sin^3\theta^i} \left(|E_z^s|^2 + |H_z^s|^2 \right) \\ &= 2\pi \frac{1}{\sin^3\theta^i} \left(\left| \tilde{f}^e(\varphi,\theta^i,\varphi^i) \right|^2 + \left| \tilde{f}^h(\varphi,\theta^i,\varphi^i) \right|^2 \right) \end{aligned} \tag{35}$$

Figures 15 and 16 illustrate the dependence of the normalized differential scattering cross section (35) versus angle of observation φ at different angles of incidence θ^i for both *concentric* and *eccentric* configuration of the cylindrical EBG structures, when the circular rods are dielectrics. Dielectric permittivity of the circular rods is $\varepsilon_1 = \varepsilon_2 = \varepsilon_3 = 4.0\varepsilon_0$. In Figure 15 we have assumed that an angle of polarization of an incident electric field is $\psi^i = 0^\circ$, which means that the incident field is TM polarized plane wave ($\mathbf{b}^{e(N)} \neq 0$, $\mathbf{b}^{h(N)} = 0$), whereas in Figure 16 an angle of polarization of the incident electric field is $\psi^i = 90^\circ$, which means that the incident field is TE polarized plane wave ($\mathbf{b}^{e(N)} = 0$, $\mathbf{b}^{h(N)} \neq 0$). In Figures 15(b), 15(d) and 16(b), 16(d) we could see that the cross-polarization scattering effect is substantial at the low angles of oblique

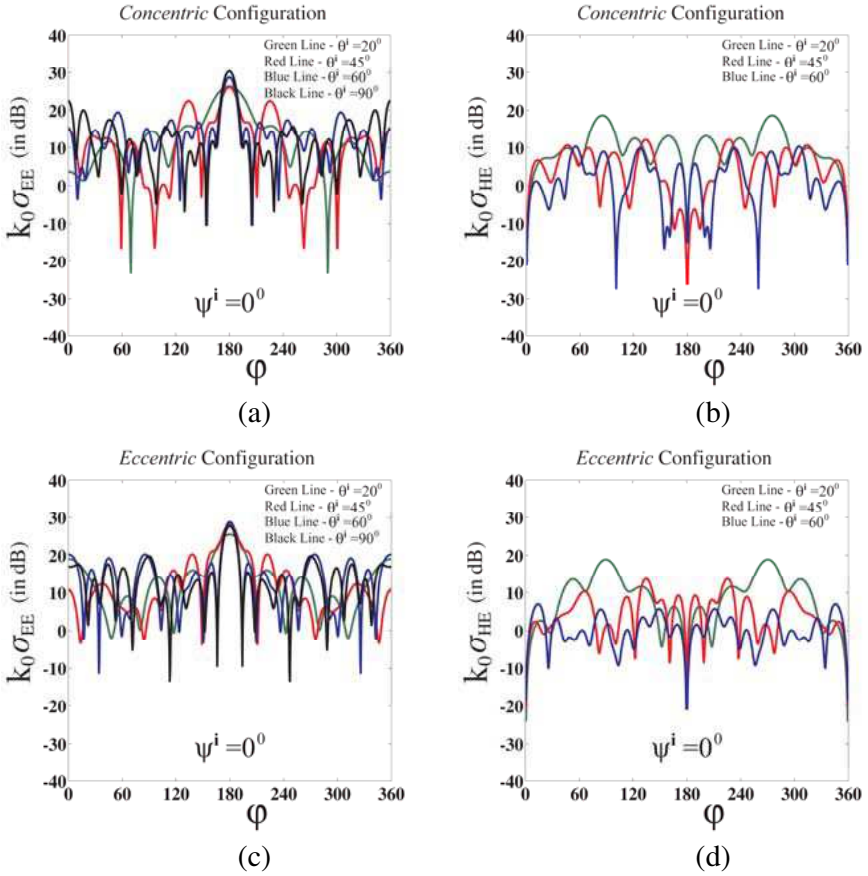

Figure 15. Normalized differential scattering cross section of (a), (c) co-polarized $k_0\sigma_{EE}$ and (b), (d) cross-polarized $k_0\sigma_{HE}$ space-harmonics versus angle of observation φ at oblique incidence of TM plane waves ($\psi^i = 0°$) on 3-layered *concentric* and *eccentric* configuration of cylindrical EBG structures composed of 8 dielectric circular rods ($\varepsilon_1 = \varepsilon_2 = \varepsilon_3 = 4.0\varepsilon_0$, $r_1 = r_2 = r_3 = 0.15R_1$) periodically distributed along each layer having radii R_1, $R_2 = 2R_1$, $R_3 = 3R_1$. Green line — $\theta^i = 20°$; red line — $\theta^i = 45°$; blue line — $\theta^i = 60°$; black line — $\theta^i = 90°$.

incidence $\theta^i = 20°$ (green line) and $\theta^i = 45°$ (red line) for both configurations of cylindrical EBG structures and polarization angle ψ^i of the incident field. The normalized differential scattering cross-sections $k_0\sigma_{HE}$ and $k_0\sigma_{EH}$ for the cross-polarized space-harmonics are almost 20 dB around $\varphi = 90°$, $270°$ at $\theta^i = 20°$. Note that cross-

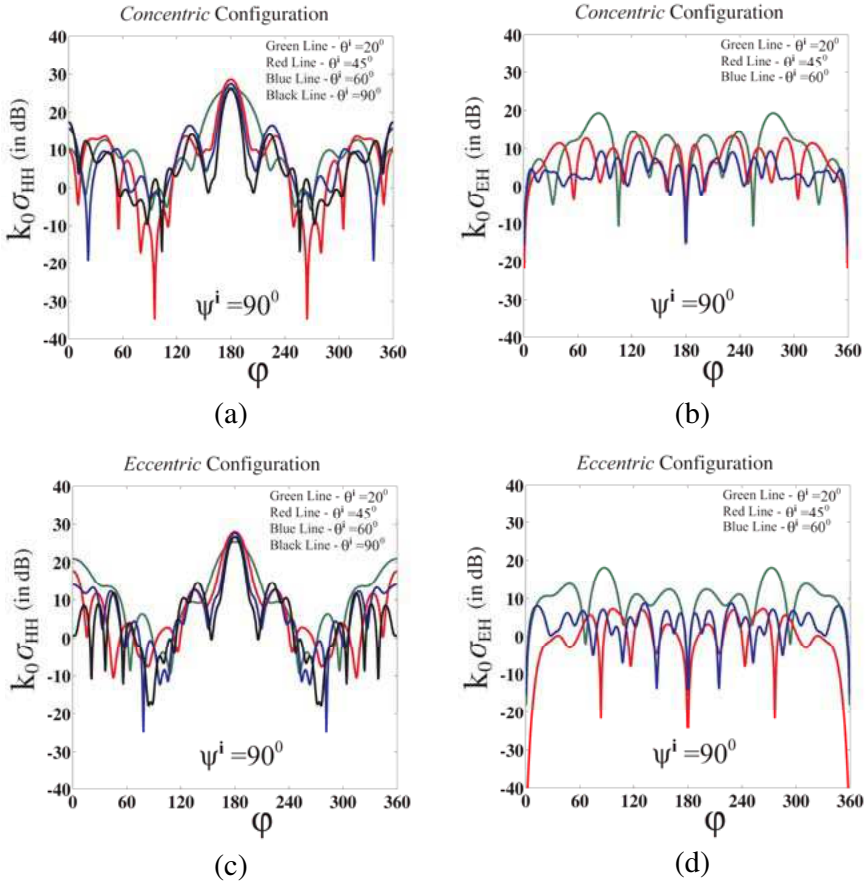

Figure 16. Normalized differential scattering cross section of (a), (c) co-polarized $k_0\sigma_{HH}$ and (b), (d) cross-polarized $k_0\sigma_{EH}$ space-harmonics versus angle of observation φ at oblique incidence of TE plane waves ($\psi^i = 90°$) on 3-layered *concentric* and *eccentric* configuration of cylindrical EBG structures. Other parameters are the same as in Figure 15.

polarization scattering effect disappears in case of normal incidence of plane waves when $\theta^i = 90°$. The results are not presented here, however it should be mentioned that the cross-polarization effect becomes very small in the lower frequency range, when $R_1/\lambda < 0.4$. As for the co-polarized scattering cross-sections $k_0\sigma_{EE}$ and $k_0\sigma_{HH}$, strong directive peaks in the forward direction $\varphi = 180°$ in the range of 25 dB–35 dB could be observed at different angles of oblique incidence θ^i for both configurations of cylindrical EBG structure and polarization angle ψ^i.

From the comparison of *concentric* and *eccentric* configurations, one distinguishable feature appears at the low angle of oblique incidence $\theta^i = 20°$ (green line), when the strong enhancement in the backward direction is observed for *eccentric* configuration.

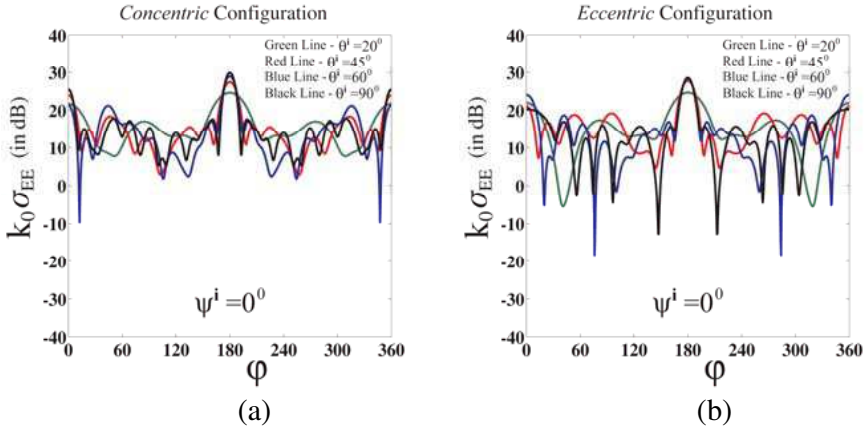

Figure 17. Normalized differential scattering cross section of co-polarized $k_0\sigma_{EE}$ space-harmonics versus angle of observation φ at oblique incidence of TM plane waves ($\psi^i = 0°$) on 3-layered (a) *concentric* and (b) *eccentric* configuration of cylindrical EBG structures composed of 8 perfect conductor circular rods ($r_1 = r_2 = r_3 = 0.15R_1$) periodically distributed along each layer having radii R_1, $R_2 = 2R_1$, $R_3 = 3R_1$. Green line — $\theta^i = 20°$; red line — $\theta^i = 45°$; blue line — $\theta^i = 60°$; black line — $\theta^i = 90°$.

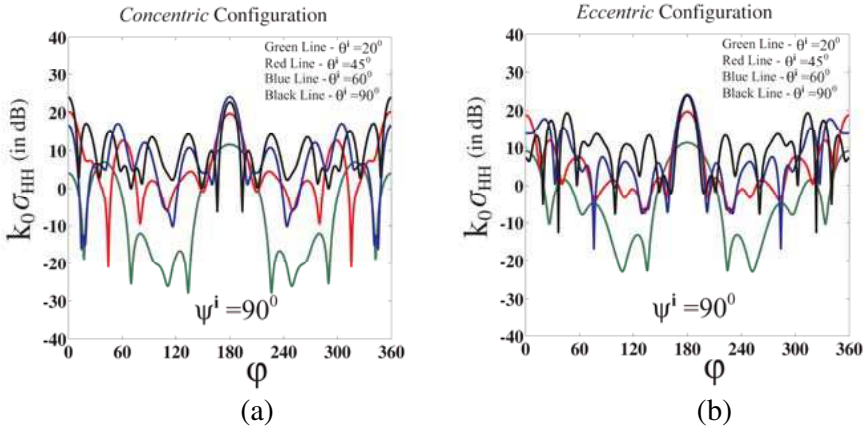

Figure 18. The same as in Figure 17 but at oblique incidence of TE plane waves ($\psi^i = 90°$).

The normalized differential scattering cross section both *concentric* and *eccentric* configuration of the cylindrical EBG structures, when the circular rods are perfect conductors is shown in Figures 17 and 18. In case of perfect conductor scatterers the cross-polarizations scattering effect disappears and only co-polarized scattering effect is observed. From the comparison of the figures for *concentric* and *eccentric* configurations, it follows that scattered intensity in the forward direction is strongly enhanced for the *concentric* configuration. Scattering intensity for incident TM waves (Figure 17) is much stronger than that for TE wave incidence (Figure 18) for both configurations, which has not been observed in case of dielectric circular rods.

In order to confirm the accuracy of the presented numerical results, we have checked the optical theorem [26] for our solutions. The scattering cross section σ_s and the extinction cross section σ_e of the cylindrical structures in case of the oblique incidence are given by:

$$\sigma_s\left(\theta^i,\varphi^i\right) = \int_0^{2\pi}\left(\left|f^e\left(\varphi,\theta^i,\varphi^i\right)\right|^2 + \left|f^h\left(\varphi,\theta^i,\varphi^i\right)\right|^2\right)d\varphi \tag{36}$$

$$\sigma_e\left(\theta^i,\varphi^i\right) = -2\sin\theta^i\sqrt{\frac{\pi}{\kappa}}\mathrm{Re}\left\{(1+i)f\left(\varphi^i,\theta^i,\varphi^i\right)\right\} \tag{37}$$

where $f(\varphi,\theta^i,\varphi^i) = f^e(\varphi,\theta^i,\varphi^i)$ for TM wave incidence ($\psi^i = 0°$) and $f(\varphi,\theta^i,\varphi^i) = f^h(\varphi,\theta^i,\varphi^i)$ for TE wave incidence ($\psi^i = 90°$). The results are presented in Tables 1 and 2. It is evident that the present solutions well satisfy the optical theorem. Further evidence of

Table 1. Test of optical theorem for three layered *concentric* and *eccentric* cylindrical EBG structures presented in Figures 15 and 16 at different truncation number L, $\theta^i = 60°$.

		Concentric Cylindrical Structure		*Eccentric* Cylindrical Structure	
	L	Optical Theorem		Optical Theorem	
		$\sigma_s(\theta^i,\varphi^i)$	$\sigma_e(\theta^i,\varphi^i)$	$\sigma_s(\theta^i,\varphi^i)$	$\sigma_e(\theta^i,\varphi^i)$
TM	4	11.77152	14.97314	8.29191	13.94306
	12	34.26664	34.73267	39.49036	40.02379
	22	32.47690	32.47690	37.67755	37.67755
	25	32.47690	32.47690	37.67755	37.67755
TE	4	11.16417	12.13700	11.98860	13.01658
	12	22.29182	22.70043	21.52457	21.88859
	22	23.89935	23.89935	22.92301	22.92301
	25	23.89935	23.89935	22.92301	22.92301

Table 2. Test of optical theorem for three layered *concentric* and *eccentric* cylindrical EBG structures presented in Figures 17 and 18 at different truncation number L, $\theta^i = 60°$.

		Concentric Cylindrical Structure		*Eccentric* Cylindrical Structure	
	L	Optical Theorem		Optical Theorem	
		$\sigma_s(\theta^i, \varphi^i)$	$\sigma_e(\theta^i, \varphi^i)$	$\sigma_s(\theta^i, \varphi^i)$	$\sigma_e(\theta^i, \varphi^i)$
TM	4	10.41336	13.32741	8.00007	12.74957
	12	38.63818	38.75950	38.30615	39.01999
	22	38.57445	38.57445	36.17259	36.17259
	25	38.57445	38.57445	36.17259	36.17259
TE	4	3.72721	4.86302	5.29174	6.55746
	12	11.99529	12.40411	12.45603	12.85726
	22	12.71366	12.71366	13.63746	13.63746
	25	12.71366	12.71366	13.63746	13.63746

the validity of the proposed method is provided by comparisons with previously published computational results. By use of our computation code we can reproduce pertinent numerical results shown in [20] (Figures 5 and 6) and in [28] (Figures 6 and 7).

REFERENCES

1. Petit, R., ed., *Electromagnetic Theory of Gratings*, Springer-Verlag, Berlin, Heidelberg, 1980.
2. Yasumoto, K., *Electromagnetic Theory and Applications for Photonic Crystals*, CRC Press, New York, 2005.
3. Yasumoto, K. and K. Yoshitomi, "Efficient calculation of lattice sums for free-space periodic Green's function," *IEEE Trans. Antennas Propag.*, Vol. 47, No. 6, 1050–1055, Jun. 1999.
4. Tayeb, G. and D. Maystre, "Rigorous theoretical study of finite-size two-dimensional photonic crystals doped by microcavities," *J. Opt. Soc. Am. A*, Vol. 14, No. 12, 3323–3332, 1997.
5. Yasumoto, K., H. Toyama, and T. Kushta, "Accurate analysis of two-dimensional electromagnetic scattering from multilayered periodic arrays of circular cylinders using lattice sums technique," *IEEE Trans. Antennas Propag.*, Vol. 52, No. 10, 2603–2611, 2004.
6. Pelosi, G., A. Cocchi, and A. Monorchio, "A hybrid FEM-based procedure for the scattering from photonic crystals illuminated

by a Gaussian beam," *IEEE Trans. Antennas Propag.*, Vol. 48, 973–980, 2000.

7. Qiu, M. and S. He, "A nonorthogonal finite-difference time-domain method for computing the band structure of a two-dimensional photonic crystal with dielectric and metallic inclusions," *Journal of Applied Physics*, Vol. 87, No. 12, 8268–8275, 2000.
8. Jandieri, V., K. Yasumoto, and B. Gupta, "Directivity of radiation from a localized source coupled to electromagnetic crystals," *International Journal of Infrared, Millimetre and Terahertz Waves*, Vol. 30, No. 10, 1102–1112, 2009.
9. Russell, P. S., "Photonic-crystal fibers," *J. Lightwave Technol.*, Vol. 24, No. 12, 4729–4749, 2006.
10. Knight, J. C., J. Broeng, T. A. Birks, and P. S. J. Russell, "Photonic band gap guidance in optical fibers," *Science*, Vol. 282, 1476–1478, 1998.
11. Boutayeb, H. and T. Denidni, "Metallic cylindrical EBG structures with defects: Directivity analysis and design optimization," *IEEE Trans. Antennas Propag.*, Vol. 55, No. 11, 3356–3361, 2007.
12. Biancotto, C. and P. Record, "Design of a beam forming dielectric cylindrical EBG antenna," *Progress In Electromagnetics Research B*, Vol. 18, 327–346, 2009.
13. Chreim, H., M. Hajj, E. Arnaud, B. Jecko, C. Dall'omo, and P. Dufrane, "Multibeam antenna for telecommunications networks using cylindrical EBG structures," *IEEE Antennas and Wireless Propagation Letters*, Vol. 8, 665–669, 2009.
14. Palikaras, G., A. Feresidis, and J. Vardaxoglou, "Cylindrical electromagnetic bandgap structures for directive base station antennas," *IEEE Antennas and Wireless Propagation Letters*, Vol. 3, 87–89, 2004.
15. Yasumoto, K. and H. Jia, "Modeling of photonic crystals by layered periodic arrays of cylinders," *Electromagnetic Theory and Applications for Photonic Crystals*, K. Yasumoto (ed.), 123–190, CRC Press, 2005.
16. Yasumoto, K., V. Jandieri, and B. Gupta, "Guidance and scattering of electromagnetic waves by layered cylindrical arrays of circular rods," *Proc. IEEE Applied Electromagnetics Conference*, 1–4, Kolkata, India, 2009.
17. Jandieri, V. and K. Yasumoto, "Electromagnetic scattering by layered cylindrical arrays of circular rods," *IEEE Trans. Antennas Propag.*, Vol. 59, No. 6, 2437–2441, 2011.

18. Chew, W. C., *Waves and Fields in Inhomogeneous Media*, Van Nostrand Reinhold, New York, 1990.
19. Elsherbeni, A. and A. Kishk, "Modeling of cylindrical objects by circular dielectric and conducting cylinders," *IEEE Trans. Antennas Propag.*, Vol. 40, No. 1, 96–99, Jan. 1992.
20. Henin, B. H., M. H. Al Sharkawy, and A. Z. Elsherbeni, "Scattering of obliquely incident plane wave by an array of parallel concentric metamaterials cylinders," *Progress In Electromagnetics Research*, Vol. 77, 285–307, 2007.
21. Yasumoto, K., "Semi-analytical approach for a specific microstructured fiber," *PIERS Online*, Vol. 5, No. 1, 95–100, 2009.
22. Jandieri, V., K. Yasumoto, A. Sharma, and H. Chauhan, "Modal analysis of specific microstructured optical fibers using a model of layered cylindrical arrays of circular rods," *IEICE Trans. Electron.*, Vol. 93, No. 1, 17–23, 2010.
23. Jandieri, V. and K. Yasumoto, "Analysis of scattering from a finite array of circular cylinders using a model of layered cylindrical arrays," *Optics Communications*, Vol. 284, 4109–4113, 2011.
24. Jandieri, V., K. Yasumoto, and Y.-K. Cho, "Analysis of radiation from line source located in cylindrical electromagnetic bandgap structures with defects," *IEICE Trans. Electron.*, Vol. 94, No. 8, 1245–1252, 2011.
25. Jakoby, B., "Scattering of obliquely incident waves by an impedance cylinder with inhomogeneous bianisotropic coating," *IEEE Trans. Antennas Propag.*, Vol. 45, No. 4, 648–655, 1997.
26. Okamoto, N. and R. Yamada, "General properties of electromagnetic scattering by inhomogeneous anisotropic composite obstacles of arbitrary shape," *Journal of Applied Physics*, Vol. 44, No. 5, 2161–2165, 1973.
27. Abramowitz, M. and I. Stegun, *Handbook of Mathematical Functions*, Dover Publications, 1965.
28. Polewski, M. and J. Mazur, "Scattering by an array of conducting, lossy dielectric, ferrite and pseudochiral cylinders," *Progress In Electromagnetics Research*, Vol. 38, 283–310, 2002.
29. Jandieri, V. and K. Yasumoto, "Stopband and resonance characteristics of cylindrical electromagnetic bandgap structures," *PIERS Proceedings*, 198–202, Suzhou, China, Sep. 12–16, 2011.